

Probing Virtual ALPs by Precision Phase Measurements: Time-Varying Magnetic Field Background

Mohammad Sharifian,^{1,2,*} Moslem Zarei,^{1,2,3,4,†} Mehdi

Abdi,^{1,‡} Marco Peloso,^{3,4,§} and Sabino Matarrese,^{3,4,5,6,¶}

¹*Department of Physics, Isfahan University of Technology, Isfahan 84156-83111, Iran*

²*ICRANet-Isfahan, Isfahan University of Technology, 84156-83111, Iran*

³*Dipartimento di Fisica e Astronomia “Galileo Galilei” Università di Padova, 35131 Padova, Italy*

⁴*INFN, Sezione di Padova, 35131 Padova, Italy*

⁵*INAF - Osservatorio Astronomico di Padova, I-35122 Padova, Italy*

⁶*Gran Sasso Science Institute, I-67100 L’Aquila, Italy*

(Dated: August 4, 2021)

We propose an experimental scheme for detecting the effects of off-shell axion-like particles (ALPs) through optical cavities. In this proposed experiment, linearly polarized photons are pumped into an optical cavity where an external time-dependent magnetic field is present. The magnetic field mediates an interaction between the cavity photons and ALPs giving rise to a modification in the phase of the cavity photons. The time-dependent nature of the external magnetic field prompts a novel amplification effect which significantly enhances this phase modification. A detection scheme is then proposed to identify such axion-induced phase shifts. We find that the phase modification is considerably sensitive to the photon-ALPs coupling constants $g_{a\gamma\gamma}$ for the range of ALPs mass $2 \times 10^{-6} \text{ eV} \leq m_a \leq 6.3 \times 10^{-5} \text{ eV}$.

I. Introduction

Axion Like Particles (ALPs) appear in several extensions of the Standard Model (SM) and are prominent candidates for Dark Matter (DM) [1–3]. They can have a multitude of different coupling to the SM particles such as electrons and photons. The particular ALP predicted by the Peccei-Quinn mechanism [4–7] to dynamically solve the strong CP problem is called the QCD axion. The phenomenology of axions and ALPs is determined by their low mass and weak interactions with

*mohammadsharifian@ph.iut.ac.ir

†m.zarei@iut.ac.ir

‡mehabdi@iut.ac.ir

§marco.peloso@pd.infn.it

¶sabino.matarrese@pd.infn.it

the environment. Such weak-coupling or masses below eV make up a well-motivated part of the parameter space but they make the detection of ALPs very challenging with current experimental setups. Nevertheless, the early attempts towards detection of ALPs trace back to 1980s, see e.g. [8–10]. In particular, the interaction of ALPs with the photon has motivated experiments such as helioscope [11] and light-shining-through-walls experiments [12–14], (see e.g. Refs. [15, 16] for a review).

The photon-ALP interaction causes a difference in phase velocity between left and right-handed circularly polarized light. In some recent proposals, it has been suggested to use high-finesse Fabry-Perot cavities to accumulate and measure the resulting phase difference [17–21]. These cavity experiments are predicted to be sensitive to the ALP-photon coupling in the mass range around $10^{-14} \leq m_a \leq 10^{-9}$ eV. ALPs can also source cosmic microwave background (CMB) birefringence [22–26]. The interaction of CMB photons with ALPs induces a rotation in angle of the plane of CMB linear polarization.

In a recent work, some of us proposed a scheme to detect virtual axion-like particles (ALPs) via a spatially non-uniform magnetic field $\mathbf{B}(\mathbf{x})$ [27]. We showed that this interaction lead to an enhanced birefringence phenomenon, which could be detected as a phase difference between the cavity polarization modes. The inhomogeneity of the external magnetic field caused a momentum transfer to the vertex of the interaction. This process was well described by an effective interaction Hamiltonian that was defined in terms of the second-order S-matrix operator [28–32]. We chose a spatially periodic magnetic field $\mathbf{B}(\mathbf{x}) \propto \mathbf{B}_0 \cos(x/\ell)$ along the cavity axis (x -direction) with the wavelength ℓ . In obtaining the effective Hamiltonian describing this process, we integrated over the volume of the cavity. Due to the presence of $\cos(x/\ell)$, integrating over x gave rise to a sinc-like profile. Therefore, in the final expression for the effective Hamiltonian we are left with an integral over k_x , with the integrand that was given by multiplying the propagator of the ALP and the profile function. The profile function developed two narrow peaks around $k_x \sim p_x \pm 1/\ell$ where k_x (p_x) was the ALP (photon) momentum. It was shown that adjusting the photon momentum entering the cavity and the wavelength ℓ around these peaks amplified the phase difference significantly, such that it could be potentially measured by the cavity experiment scheme.

In this paper, we instead consider photons in an optical cavity interacting with a time-dependent external magnetic field $\mathbf{B}(t)$ mediated by an off-shell ALP. Due to the time dependence of the external magnetic field, energy is transferred to the interaction vertex. Here, a harmonic magnetic field $\mathbf{B}(t) \propto \mathbf{B}_0 \cos(\omega_B t)$ with angular frequency ω_B is considered. Due to the presence of this oscillating magnetic field, a profile function depending on the frequency of the magnetic field and

the energy of the input photons is developed in the interaction Hamiltonian. We shall show that in addition to the Breit-Wigner enhancement [33], the profile also induces a novel amplification effect. We provide an analytical expression for the effect of the resonance, and corroborate it with the numerical results for the impact of the resonance on the phase.

The detection scheme benefits from a noise cancellation mechanism where the phase destroying effects such as thermal vibrations of the cavity walls, as well as the pump laser phase noise are eliminated. For this, we propose to employ a Fabry-Perot cavity inside a time-varying uniform magnetic field. The cavity is aligned such that the direction of propagation of the photons inside the cavity is perpendicular to \mathbf{B} . In the regime in which the electric field induced by the time-varying magnetic field is negligible, only the cavity polarizations component which is aligned to the magnetic field is affected by the ALP, while the polarization mode which is perpendicular to the magnetic field remains unaffected. Hence, by equally pumping both cavity polarization modes the axion-induced phase difference accumulated at the outgoing cavity field is detected via a balanced Homodyne measurement where both output modes are combined through a 50:50 beam-splitter and then observed by two photodetectors [34].

The paper is organized as follows: In Section II we provide a detailed calculation of the Hamiltonian describing the interaction of photons with a time-dependent magnetic field mediated by ALP. In Section III we deal with the cavity detection scheme and calculate the phase difference between cavity polarization modes. We will also present an analytical study of the new enhancement effect in this section. Section IV is devoted to discussing the sensitivity of our cavity experiment that results in the exclusion region in the ALPs parameters. Finally, Section V presents our conclusions.

II. Impacts of the ALP-photon scattering on the cavity polarization modes

The scattering process of photons off external time-dependent magnetic field $\mathbf{B}(t)$ mediated by an off-shell ALP develops a phase difference between the cavity polarization modes. It turns out that the periodicity of $\mathbf{B}(t)$ amplifies this effect. In this section, we investigate this scattering phenomenon in detail.

The following Lagrangian describes the axion-photon interaction

$$\mathcal{L}_{a\gamma\gamma} = \frac{1}{4} g_{a\gamma\gamma} \phi F_{\mu\nu} \tilde{F}^{\mu\nu} , \quad (1)$$

where ϕ is the ALP field, $F_{\mu\nu}$ is the electromagnetic field with $\tilde{F}^{\mu\nu} = \frac{1}{2} \epsilon^{\mu\nu\rho\sigma} F_{\rho\sigma}$ its dual, and $g_{a\gamma\gamma}$ is the coupling constant. Since we are interested in an ALP-mediated process in an external magnetic

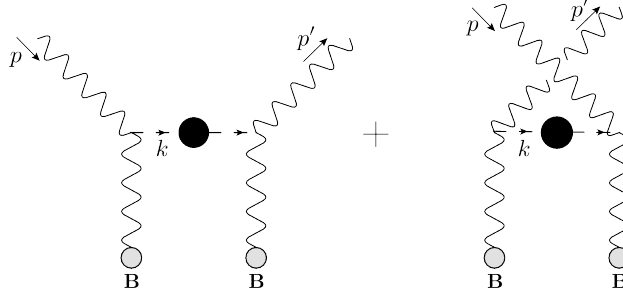


FIG. 1: Two Feynman diagrams corresponding to the scattering process.

field, we split the tensor $F_{\mu\nu}$ into a homogeneous background $\bar{F}_{\mu\nu}$ and a fluctuating quantum part $f_{\mu\nu} = \partial_\mu A_\nu - \partial_\nu A_\mu$ with A_μ denoting the photon field. Therefore, by expanding the interaction term about the background one arrives at the following Lagrangian

$$\mathcal{L}_{a\gamma\gamma} = \frac{1}{2} g_{a\gamma\gamma} \phi \epsilon^{\mu\nu\rho\sigma} \bar{F}_{\mu\nu} \partial_\rho A_\sigma . \quad (2)$$

This interaction Lagrangian allows us to investigate the interaction of a propagating polarized photon with a time-dependent background magnetic field through the intermediate ALP field. Fig. (1) illustrates the two Feynman diagrams associated with such process. The effective interaction Hamiltonian is found through the S-matrix operator associated with this process [28]

$$S^{(2)}(\gamma_s \rightarrow \gamma_{s'}) = -i \int dt H(t) , \quad (3)$$

where $H(t)$ describing the process shown in Fig. (1) is given by

$$H(t) = \frac{g_{a\gamma\gamma}^2}{8} \int d^4x' d^3x \epsilon^{\mu\nu\rho\sigma} \epsilon^{\mu'\nu'\rho'\sigma'} \bar{F}_{\rho\sigma}(x) \bar{F}_{\rho'\sigma'}(x') D_F(x-x') [\partial_\mu A_\nu^-(x) \partial_{\mu'} A_{\nu'}^+(x') + \partial_{\mu'} A_{\nu'}^-(x') \partial_\mu A_\nu^+(x)] . \quad (4)$$

Here, $D_F(x-x')$ is the Breit-Wigner Feynman propagator for the ALP, and A_μ^+ (A_μ^-) is the electromagnetic field linear in the absorption (creation) operators of the photons. It is worth mentioning that due to the time-dependence of the external magnetic field, an electric field is induced as implied by Faraday's law $\nabla \times \mathbf{E} = -\frac{\partial}{\partial t} \mathbf{B}$. Therefore, one must keep both magnetic field $B^k(t) = -\epsilon^{kij} \bar{F}_{ij}/2$ and electric field $E_i = F_{0i}$ contributions in the interaction Hamiltonian (4). However, as we shall discuss below, the induced electric field can be made negligible by a proper choice of setup parameters.

We consider a one-dimensional cavity. This is effectively realized by taking one direction of the cavity walls, say L_x , to be much smaller than the other two, L_y and L_z . We inject in the cavity a time dependent background magnetic field aligned along the z -direction. To estimate the induced

electric field inside the cavity, we start from Faraday's law,

$$\nabla \times \mathbf{E} = -\frac{\partial \mathbf{B}}{\partial t} , \quad (5)$$

and write parametrically $\nabla \times \mathbf{E} \sim E_0/L_x$ in which E_0 is the amplitude of the induced electric field and L_x is the smallest length scale of the cavity. For an oscillating magnetic field of the angular frequency ω_B and the amplitude B_0 we can also write $\frac{\partial \mathbf{B}}{\partial t} \sim B_0 \omega_B$. Therefore, one can estimate the induced electric field as

$$\frac{E_0}{B_0} \sim 3.2 \times 10^{-4} \frac{\omega_B}{1 \text{ MHz}} \frac{L_x}{10 \text{ cm}} . \quad (6)$$

For $\omega_B \sim 10$ MHz, having a cavity with $L_x \lesssim 100$ cm guarantees subdominant induced electric field. Otherwise, for larger cavity lengths the electric field becomes significant, and it must be involved in the interaction Hamiltonian. In this work, we only take parameter ranges that the electric field can be neglected.

To evaluate the Hamiltonian (4) in this background magnetic field, we quantize the photon field A in the coulomb gauge, $A^0 = 0$. The photon field quantization in a cavity formed by perfectly conducting walls has been discussed in [35]. Here we only assume that the smaller length L_x is bounded by two conducting walls, while we treat the other dimensions as unbounded (consistently with the $L_y = L_z \gg L_x$ setup). The boundary conditions on $\mathbf{A}(x)$ are thus applied so that the tangential component of the electric field associated with $\mathbf{A}(x)$ and the normal component of the magnetic field associated with $\mathbf{A}(x)$ must vanish at the cavity boundaries in this direction. By imposing these boundary conditions, we arrive at

$$\mathbf{A}(x) = \sum_s \sum_{\mathbf{p}} \frac{1}{\sqrt{\omega_{\mathbf{p}} V}} \left[a_s(\mathbf{p}) \mathbf{u}_s(\mathbf{p}) + a_s^\dagger(\mathbf{p}) \mathbf{u}_s^*(\mathbf{p}) \right] , \quad (7)$$

where the mode functions are given by

$$\mathbf{u}_s(\mathbf{p}) = (\cos(p_x x) \varepsilon_s^x(\mathbf{p}), i \sin(p_x x) \varepsilon_s^y(\mathbf{p}), i \sin(p_x x) \varepsilon_s^z(\mathbf{p})) e^{ip_y y} e^{ip_z z} e^{-i\omega_{\mathbf{p}} t} , \quad (8)$$

where ε_s is the photon polarization, $\mathbf{p} = (p_x, p_y, p_z) = \left(\frac{\pi l_1}{L_x}, \frac{2\pi l_2}{L_y}, \frac{2\pi l_3}{L_z} \right)$ with $l_2, l_3 = 0, \pm 1, \pm 2, \dots$ and $l_1 = 0, 1, 2, \dots$. In Eq. (7) we also have annihilation and creation operators of the photons with polarization s and momentum \mathbf{p} , that satisfy

$$\left[a_s(\mathbf{p}), a_{s'}^\dagger(\mathbf{p}') \right] = \delta_{ss'} \delta_{\mathbf{p}, \mathbf{p}'} . \quad (9)$$

Finally, $\omega_{\mathbf{p}} = |\mathbf{p}|$ is the photon angular frequency, while V is the cavity volume.

Inserting the expression (7) in Eq. (4), and assuming a background magnetic field, results in two scalar products between the magnetic field and the polarization vector of $\mathbf{A}(x)$. Since the magnetic field is oriented along the z -direction, we can effectively replace (7) with the simpler

$$\mathbf{A}(x) = \mathbf{A}^+(x) + \mathbf{A}^-(x) = \sum_s \sum_{\mathbf{p}} \frac{1}{\sqrt{\omega_{\mathbf{p}} V}} [i \sin(p_x x) a_s(\mathbf{p}) e^{ip_y y} e^{ip_z z} e^{-i\omega_{\mathbf{p}} t} \varepsilon_s^z(\mathbf{p}) + \text{h.c.}] \quad (10)$$

Eq. (4) then evaluates to

$$\begin{aligned} H(t) &= \frac{g_{a\gamma\gamma}^2}{2V} \sum_{s,s'} \sum_{\mathbf{p},\mathbf{p}'} \sqrt{\omega_{\mathbf{p}} \omega_{\mathbf{p}'}} \int dt' dx' d^2 \mathbf{x}'_{\perp} dx d^2 \mathbf{x}_{\perp} \frac{d^4 k}{(2\pi)^4} D_F(k) [\varepsilon_s(\mathbf{p}) \cdot \mathbf{B}(t)] [\varepsilon_{s'}^*(\mathbf{p}') \cdot \mathbf{B}(t')] \\ &\times a_{s'}^{\dagger}(\mathbf{p}') a_s(\mathbf{p}) \left[\sin(p'_x x) \sin(p_x x') e^{-i\mathbf{k} \cdot \mathbf{x}'} e^{-i\mathbf{p}'_{\perp} \cdot \mathbf{x}_{\perp}} e^{i\mathbf{k} \cdot \mathbf{x}} e^{i\mathbf{p}_{\perp} \cdot \mathbf{x}_{\perp}} e^{-i(-k^0 + \omega_{\mathbf{p}})t'} e^{-i(k^0 - \omega_{\mathbf{p}'})t} \right. \\ &+ \left. \sin(p'_x x') \sin(p_x x) e^{-i\mathbf{k} \cdot \mathbf{x}'} e^{-i\mathbf{p}'_{\perp} \cdot \mathbf{x}_{\perp}} e^{i\mathbf{k} \cdot \mathbf{x}} e^{i\mathbf{p}_{\perp} \cdot \mathbf{x}_{\perp}} e^{-i(-k^0 - \omega_{\mathbf{p}'})t'} e^{-i(k^0 + \omega_{\mathbf{p}})t} \right] , \end{aligned} \quad (11)$$

where $D_F(k)$ is the Fourier transform of $D_F(x)$, which is defined by

$$D_F(x - x') = \int \frac{d^4 k}{(2\pi)^4} \frac{i}{k^2 - m_a^2 + ik^0 \Gamma_B(k^0)} e^{-ik \cdot (x - x')} , \quad (12)$$

in which m_a is the ALP physical mass, and $\Gamma_B(k^0)$ is the ALP decay rate in the presence of a time-dependent magnetic field and has been derived in Appendix A.

A. Time-dependent magnetic field

The central quantity for describing the process described above is the interaction Hamiltonian $H(t)$, defined from the S-matrix. Therefore, it is crucial to construct well-separated in and out states with the specified content in the far past and future. The in and out states must be time-independent. This cannot be realized in the presence of a time-dependent background field. We consider a setup where the interaction between photon and background field is turned on (off) at $-\frac{1}{2}\tau_B$ ($+\frac{1}{2}\tau_B$). Therefore, the time-dependent magnetic field is considered as the form

$$\mathbf{B}(t) = \mathbf{B}_0 \cos \omega_B t \Pi\left(\frac{t}{\tau_B}\right) , \quad \mathbf{B}_0 = B_0(0, 0, 1) \quad (13)$$

where $\Pi(t/\tau_B)$ is a rectangular function centered at $t = 0$ that models the time duration τ_B in which the magnetic field is applied. We will also compare our results with a smoother approximation of $\Pi(t/\tau_B)$ that is closer to the real conditions.

An optimal condition is obtained when the $\cos \omega_B t$ term oscillates several times in the τ_B interval. This condition is met for $1/\omega_B \ll \tau_B$. Moreover, since we want to make sure that the magnetic field triggers from zero, τ_B should be as $\tau_B = (2n + 1)\pi/\omega_B$ in which n is a natural

number that must be $n \gg 1$ to satisfy the condition $1/\omega_B \ll \tau_B$. Now, inserting (13) in the interaction Hamiltonian (11), carrying out the integration over \mathbf{x}_\perp , \mathbf{x}'_\perp and \mathbf{k}_\perp yields

$$\begin{aligned}
H(t) = & \frac{g_{a\gamma\gamma}^2}{2V} \cos(\omega_B t) \Pi\left(\frac{t}{\tau_B}\right) \sum_{s,s'} \sum_{\mathbf{p},\mathbf{p}'} \sqrt{\omega_{\mathbf{p}}\omega_{\mathbf{p}'}} \left[\boldsymbol{\varepsilon}_{s'}^*(\mathbf{p}') \cdot \mathbf{B}_0\right] \left[\boldsymbol{\varepsilon}_s(\mathbf{p}) \cdot \mathbf{B}_0\right] a_{s'}^\dagger(\mathbf{p}') a_s(\mathbf{p}) \\
& \times \int dt' dx' dx \frac{dk^0}{2\pi} \frac{dk_x}{2\pi} \cos(\omega_B t') \Pi\left(\frac{t'}{\tau_B}\right) \frac{1}{k^0{}^2 - m_a^2 - k_x^2 - \mathbf{p}_\perp^2 + ik^0\Gamma_B(k^0)} (2\pi)^2 \delta^2(\mathbf{p}_\perp - \mathbf{p}'_\perp) \\
& \times \left[\sin(p'_x x) \sin(p_x x') e^{-ik_x x'} e^{ik_x x} e^{-i(-k^0 + \omega_{\mathbf{p}})t'} e^{-i(k^0 - \omega_{\mathbf{p}'})t} \right. \\
& \left. + \sin(p'_x x') \sin(p_x x) e^{-ik_x x'} e^{ik_x x} e^{-i(-k^0 - \omega_{\mathbf{p}'})t'} e^{-i(k^0 + \omega_{\mathbf{p}})t} \right]. \quad (14)
\end{aligned}$$

By replacing the Dirac delta function with the discrete Kronecker delta function as $(2\pi)^2 \delta^2(\mathbf{p}_\perp - \mathbf{p}'_\perp) = L_y L_z \delta_{\mathbf{p}_\perp, \mathbf{p}'_\perp}^2$ and after integrating over t' we find

$$\begin{aligned}
H(t) = & \frac{g_{a\gamma\gamma}^2}{2L_x} \cos(\omega_B t) \Pi\left(\frac{t}{\tau_B}\right) \sum_{s,s'} \sum_{\mathbf{p},\mathbf{p}'_x} \sqrt{\omega_{\mathbf{p}}\omega_{\mathbf{p}'}} \left[\boldsymbol{\varepsilon}_{s'}^*(\mathbf{p}') \cdot \mathbf{B}_0\right] \left[\boldsymbol{\varepsilon}_s(\mathbf{p}) \cdot \mathbf{B}_0\right] a_{s'}^\dagger(\mathbf{p}') a_s(\mathbf{p}) \\
& \times \int \frac{dk^0}{2\pi} \frac{dk_x}{2\pi} \frac{1}{k^0{}^2 - m_a^2 - k_x^2 - \mathbf{p}_\perp^2 + ik^0\Gamma_B(k^0)} \\
& \times \left[\int_0^{L_x} dx \sin(p'_x x) e^{-ik_x x} \int_0^{L_x} dx' \sin(p_x x') e^{ik_x x'} P_1(k^0) e^{-i(k^0 - \omega_{\mathbf{p}'})t} \right. \\
& \left. + \int_0^{L_x} dx \sin(p_x x) e^{-ik_x x} \int_0^{L_x} dx' \sin(p'_x x') e^{ik_x x'} P_2(k^0) e^{-i(k^0 + \omega_{\mathbf{p}})t} \right]. \quad (15)
\end{aligned}$$

where

$$P_1(k^0) = \int_{-\infty}^{\infty} dt' \cos(\omega_B t') \Pi\left(\frac{t'}{\tau_B}\right) e^{-i(-k^0 + \omega_{\mathbf{p}})t'} = \frac{\sin(\Delta_1 \tau_B/2)}{\Delta_1} + \frac{\sin(\Delta_2 \tau_B/2)}{\Delta_2}, \quad (16)$$

and

$$P_2(k^0) = \int_{-\infty}^{\infty} dt' \cos(\omega_B t') \Pi\left(\frac{t'}{\tau_B}\right) e^{-i(-k^0 - \omega_{\mathbf{p}})t'} = \frac{\sin(\Delta_3 \tau_B/2)}{\Delta_3} + \frac{\sin(\Delta_4 \tau_B/2)}{\Delta_4}, \quad (17)$$

with $\Delta_1 = k^0 + \omega_B - \omega_{\mathbf{p}}$, $\Delta_2 = k^0 - \omega_B - \omega_{\mathbf{p}}$ and $\Delta_3 = k^0 + \omega_B + \omega_{\mathbf{p}}$ and $\Delta_4 = k^0 - \omega_B + \omega_{\mathbf{p}}$. The *sinc* functions in (16) and (17) appear due to the rectangular form that we have considered for the magnetic field pulse, $\Pi(t/\tau_B)$. In appendix C, we replace $\Pi(t/\tau_B)$ with a smoother function and compute (16) numerically. Our numerical investigations assure that considering a rectangular profile with smoothened edges (see dashed curves in Fig. (8a)) does not affect the results obtained below, using Eqs. (16) and (17).

Assuming that the wavelength of the photons inside the cavity is much smaller than the length of the cavity, $\lambda/L_x \ll 1$, one can approximately write the results of the integration over x and x' in terms of the Dirac delta function

$$\begin{aligned}
\int_0^{L_x} dx \sin(p_x x) e^{-ik_x x} \int_0^{L_x} dx' \sin(p'_x x') e^{ik_x x'} & \rightarrow \frac{\pi^2}{4} [\delta(k_x + p_x) - \delta(k_x - p_x)] [\delta(k_x + p'_x) \\
& - \delta(k_x - p'_x)]. \quad (18)
\end{aligned}$$

Substituting (18) into (15) and integrating over k_x we obtain

$$\begin{aligned}
H(t) = & \frac{g_{a\gamma\gamma}^2}{2L_x} \cos(\omega_B t) \Pi\left(\frac{t}{\tau_B}\right) \sum_{s,s'} \sum_{\mathbf{p}, \mathbf{p}'_x} \sqrt{\omega_{\mathbf{p}} \omega_{\mathbf{p}'}} \left[\boldsymbol{\varepsilon}_{s'}^*(\mathbf{p}') \cdot \mathbf{B}_0 \right] \left[\boldsymbol{\varepsilon}_s(\mathbf{p}) \cdot \mathbf{B}_0 \right] a_{s'}^\dagger(\mathbf{p}') a_s(\mathbf{p}) \\
& \times \int_{-\infty}^{\infty} \frac{dk^0}{2\pi} \frac{1}{k^{02} - m_a^2 - p_x^2 - \mathbf{p}_\perp^2 + ik^0 \Gamma_B(k^0)} \frac{\pi}{8} (\delta(p_x - p'_x) - \delta(p_x + p'_x) - \delta(p'_x + p_x) \\
& + \delta(p'_x - p_x)) \times \left[P_1(k^0) e^{-i(k^0 - \omega_{\mathbf{p}'})t} + P_2(k^0) e^{-i(k^0 + \omega_{\mathbf{p}})t} \right]. \tag{19}
\end{aligned}$$

Exploiting the discrete form of delta function relation $2\pi\delta(p_x - p'_x) = L_x \delta_{p_x, p'_x}$, we get

$$\begin{aligned}
H(t) = & \frac{g_{a\gamma\gamma}^2}{2L_x} \cos(\omega_B t) \Pi\left(\frac{t}{\tau_B}\right) \sum_{s,s'} \sum_{\mathbf{p}, \mathbf{p}'_x} \sqrt{\omega_{\mathbf{p}} \omega_{\mathbf{p}'}} \left[\boldsymbol{\varepsilon}_{s'}^*(\mathbf{p}') \cdot \mathbf{B}_0 \right] \left[\boldsymbol{\varepsilon}_s(\mathbf{p}) \cdot \mathbf{B}_0 \right] a_{s'}^\dagger(\mathbf{p}') a_s(\mathbf{p}) \\
& \times \int_{-\infty}^{\infty} \frac{dk^0}{2\pi} \frac{1}{k^{02} - m_a^2 - p_x^2 - \mathbf{p}_\perp^2 + ik^0 \Gamma_B(k^0)} \frac{L_x}{16} (\delta_{p_x, p'_x} - \delta_{p_x, -p'_x} - \delta_{-p_x, p'_x} + \delta_{p_x, p'_x}) \\
& \times \left[P_1(k^0) e^{-it(k^0 - \omega_{\mathbf{p}'})} + P_2(k^0) e^{-it(k^0 + \omega_{\mathbf{p}})} \right], \tag{20}
\end{aligned}$$

that can be expressed as

$$H(t) = \sum_{s,s'} \sum_{\mathbf{p}} \mathcal{F}(t) \left[\boldsymbol{\varepsilon}_{s'}^*(\mathbf{p}) \cdot \hat{\mathbf{b}} \right] \left[\boldsymbol{\varepsilon}_s(\mathbf{p}) \cdot \hat{\mathbf{b}} \right] a_{s'}^\dagger(\mathbf{p}) a_s(\mathbf{p}), \tag{21}$$

where $\hat{\mathbf{b}}$ is the direction of magnetic field and $\mathcal{F}(t)$ is

$$\begin{aligned}
\mathcal{F}(t) = & G_a \cos(\omega_B t) \Pi\left(\frac{t}{\tau_B}\right) \omega_{\mathbf{p}} \int_{-\infty}^{\infty} dk^0 \frac{1}{k^{02} - \tilde{\omega}_{\mathbf{p}}^2 + ik^0 \Gamma_B(k^0)} \left[e^{-it(k^0 - \omega_{\mathbf{p}})} P_1(k^0) \right. \\
& \left. + e^{-it(k^0 + \omega_{\mathbf{p}})} P_2(k^0) \right], \tag{22}
\end{aligned}$$

where $G_a = \frac{g_{a\gamma\gamma}^2 B_0^2}{32\pi}$ and $\tilde{\omega}_{\mathbf{p}}^2 = \omega_{\mathbf{p}}^2 + m_a^2$.

The function $\mathcal{F}(t)$ entering in the Hamiltonian (21) is a time-dependent coupling that as we show below causes an enhancement effect in the phase difference between two polarizations of the photons inside the cavity.

III. Cavity detection scheme

Our strategy for tracing polarization flips induced by the ALPs is to use high-finesse cavities and high-precision phase measurement schemes. This is schematically illustrated in Fig. (2); a Fabry-Perot optical cavity of length L_x is placed in an external time-dependent magnetic field that is perpendicular to the cavity axis. A high-frequency magnetic field, that satisfies the resonance conditions discussed below, influences the cavity fields in a birefringence fashion.

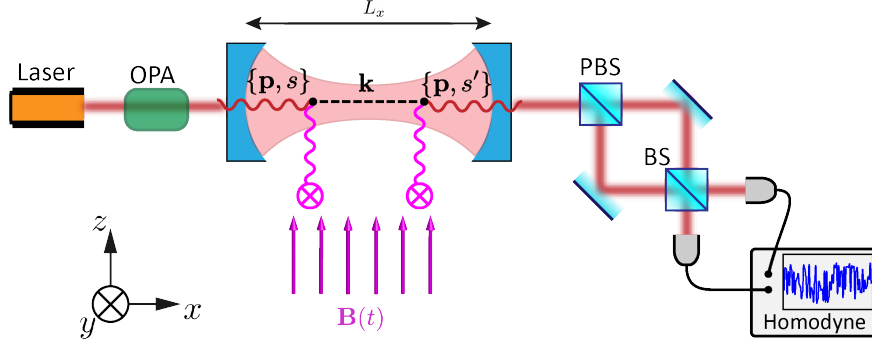


FIG. 2: The schematic diagram of setup proposed in this paper: An optical cavity of length L_x is pumped by coherent or squeezed light. A background magnetic field is applied perpendicularly to the cavity axis, mediating the laser interaction with ALPs. The axion-induced dispersion introduces a phase deviation which is measured through a homodyne detection.

The Hamiltonian of our system is given by

$$H_S = \sum_{s=1,2} \sum_{\mathbf{p}} \omega_{\mathbf{p}} a_s^\dagger(\mathbf{p}) a_s(\mathbf{p}) , \quad (23)$$

describing doubly degenerate cavity modes with two orthogonal polarizations. In the presence of an oscillating magnetic field, ALPs interact with the cavity modes depending on the angle of their polarization vector with respect to the magnetic field: A full alignment leads to the maximum interaction, while a photon polarized perpendicular to the magnetic field is unaffected. Without loss of generality, we consider a geometry where only one of the polarization modes ‘feels’ the ALPs through our proposed interaction scheme, and the other degenerate perpendicular polarization is employed as a phase reference, see Fig. (3). The total interaction Hamiltonian is thus written as

$$H_{\text{int}} = \sum_{\mathbf{q}} \mathcal{F}(t) a_1^\dagger(\mathbf{q}) a_1(\mathbf{q}) , \quad (24)$$

where we denoted by \mathbf{q} the momentum in this expression, not to confuse it with the momentum \mathbf{p} of the cavity photons in the experiment. We can now use this interaction Hamiltonian to study the time evolution of the cavity photons of momentum \mathbf{p} . The environmental effects are taken into account as dissipation and fluctuations in the modes following the standard input-output theory [34, 36, 37]. Starting from the Langevin-Heisenberg equation for the system operators

$$\frac{da_i(\mathbf{p})}{dt} = -i[a_i(\mathbf{p}), H_S + H_{\text{int}}] - \kappa a_i(\mathbf{p}) + \sqrt{2\kappa} a_i^{\text{in}} , \quad (25)$$

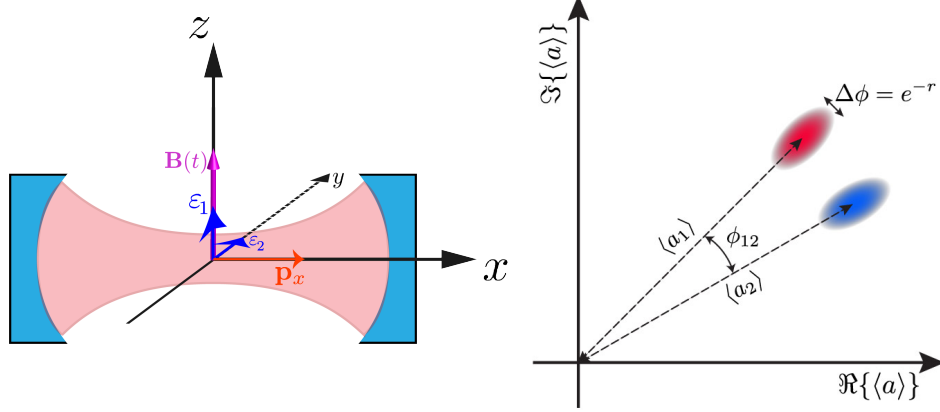


FIG. 3: The polarization vectors are chosen to be in the y and z directions (left). The phase space diagram of the two polarization modes (right).

we arrive at the following Langevin equations for the cavity mode operators

$$\dot{a}_1(\mathbf{p}) = -[\bar{\kappa} + i\bar{\omega}_{\mathbf{p}}] a_1(\mathbf{p}) + \sqrt{2\bar{\kappa}} a_1^{\text{in}} , \quad (26a)$$

$$\dot{a}_2(\mathbf{p}) = -[\kappa + i\omega_{\mathbf{p}}] a_2(\mathbf{p}) + \sqrt{2\kappa} a_2^{\text{in}} , \quad (26b)$$

where a_i^{in} is the input field operator, $\bar{\kappa}$ and $\bar{\omega}_{\mathbf{p}}$ are defined as

$$\bar{\kappa} = \kappa - \mathcal{F}_i , \quad \bar{\omega}_{\mathbf{p}} = \omega_{\mathbf{p}} + \mathcal{F}_r , \quad (27)$$

in which κ is the bare coupling of the system and the environment known as the cavity decay rate. This parameter determines the photon lifetime (the typical time spent by the photons inside the cavity) through $\tau = 1/\kappa$. Now, a laser pulse on-resonance with one of the cavity normal frequencies $\omega_{\mathbf{p}} = n\pi c/L_x$ pumps the cavity. Here, $\pi c/L_x$ is the free spectral range (FSR) of the cavity. The equation (26a) shows that $\mathcal{F}(t)$ only affects the dynamics of the photons polarized along the magnetic field. The imaginary part of $\mathcal{F}(t)$ contributes to the cavity decay rate and potentially gives rise to the amplification of the output signal. On the other hand, the real part of $\mathcal{F}(t)$ contributes to the phase of the output signal and produces a phase difference with respect to the signal with the polarization perpendicular to the magnetic field. Eqs. (26) are solved by

$$a_1(t) = e^{-\int_{t_0}^t dt_1 (\kappa + i\omega_{\mathbf{p}} + i\mathcal{F}(t_1))} \left[a_1(t_0) + \sqrt{2\bar{\kappa}} \int_{t_0}^t e^{-i\omega_{\mathbf{p}} t_2 + \int_{t_0}^{t_2} dt_1 (\kappa + i\omega_{\mathbf{p}} + i\mathcal{F}(t_1))} a_1^{\text{in}}(t_2) dt_2 \right] , \quad (28a)$$

$$a_2(t) = e^{-\int_{t_0}^t dt_1 (\kappa + i\omega_{\mathbf{p}})} \left[a_2(t_0) + \sqrt{2\kappa} \int_{t_0}^t e^{-i\omega_{\mathbf{p}} t_2 + \int_{t_0}^{t_2} dt_1 (\kappa + i\omega_{\mathbf{p}})} a_2^{\text{in}}(t_2) dt_2 \right] . \quad (28b)$$

Below, we evaluate these equations numerically. Before doing so, however, we can study these formal solutions analytically, to get a better insight into the origin of the enhancement signal effect

that we will find numerically. We first turn to the time integration over $\mathcal{F}(t)$ that appears in (28a). For the input fields at $t_0 \rightarrow -\infty$ and the output fields at $t \rightarrow \infty$ we take integration over t_1 as

$$\varphi \equiv \int_{-\infty}^{\infty} dt_1 \mathcal{F}(t_1) = G_a \omega_{\mathbf{p}} \int_{-\infty}^{\infty} dk^0 \frac{\rho(k^0)}{k^{02} - \tilde{\omega}_{\mathbf{p}}^2 + i\gamma_B}, \quad (29)$$

where $\gamma_B = k^0 \Gamma_B^{\max}(k^0)$ and

$$\rho(k^0) = P_1^2(k^0) + P_2^2(k^0), \quad (30)$$

is a spectral density-like function. As we will show below, the integrand of (29) develops extra peaks, besides those from the propagator, due to the function $\rho(k^0)$. The pole structure of the propagator and the analytic properties of $\rho(k^0)$ around its peaks is of great importance towards understanding the enhancement effect that occurs in the axion-induced phase. The function $\rho(k^0)$ is different from the standard spectral density that appears in quantum field theory. In the standard spectral density, there is a Dirac delta function which corresponds to the existence of a one-particle state in the spectrum of the theory. This term is then followed by a second term, that has the structure of a continuum component. Here, the propagator is weighted with $\rho(k^0)$ which plays as a moderator. In Fig. (4a) we plot $\rho(k^0)$ with respect to k^0 for $\omega_{\mathbf{p}} = 10^{-5}$ eV and $\omega_B = 10$ GHz. We recognize that there are four positive sharp peaks at $k^0 = \omega_{\mathbf{p}} \pm \omega_B$ and $k^0 = -\omega_{\mathbf{p}} \pm \omega_B$. Practical ω_B with the current technology is typically smaller than $\omega_B = 10$ GHz. Hence, for $\omega_B \ll 10$ GHz, the splitting between the $\pm\omega_{\mathbf{p}} + \omega_B$ and $\pm\omega_{\mathbf{p}} - \omega_B$ peaks becomes negligible compared to their width and they merge into two peaks at $\approx \pm\omega_{\mathbf{p}}$. In Figs. (4b) and (4c), we then display, respectively, the real and the imaginary parts of the integrand in equation (29). The left and right panels show the real and imaginary parts of the integrand, respectively. In the real part, there are four sharp side peaks at $k^0 = \pm\sqrt{\tilde{\omega}_{\mathbf{p}}^2 \pm \gamma_B^2}$ produced by the poles of the propagator. The integrand changes sign on each side by moving from $\sqrt{\tilde{\omega}_{\mathbf{p}}^2 - \gamma_B^2}$ to $\sqrt{\tilde{\omega}_{\mathbf{p}}^2 + \gamma_B^2}$. In the intermediate region close to $k^0 = 0$, the profile effects become more important. In this region, four peaks corresponding to the peaks of the profile function $\rho(k^0)$ appear. The same structure is observed for the imaginary part, with the difference that the imaginary part does not change sign across the poles from the propagator.

To proceed with our analytic estimate of the solution, we first focus on the side peaks arising from the propagator. We perform an expansion of the full propagator around its poles and compute

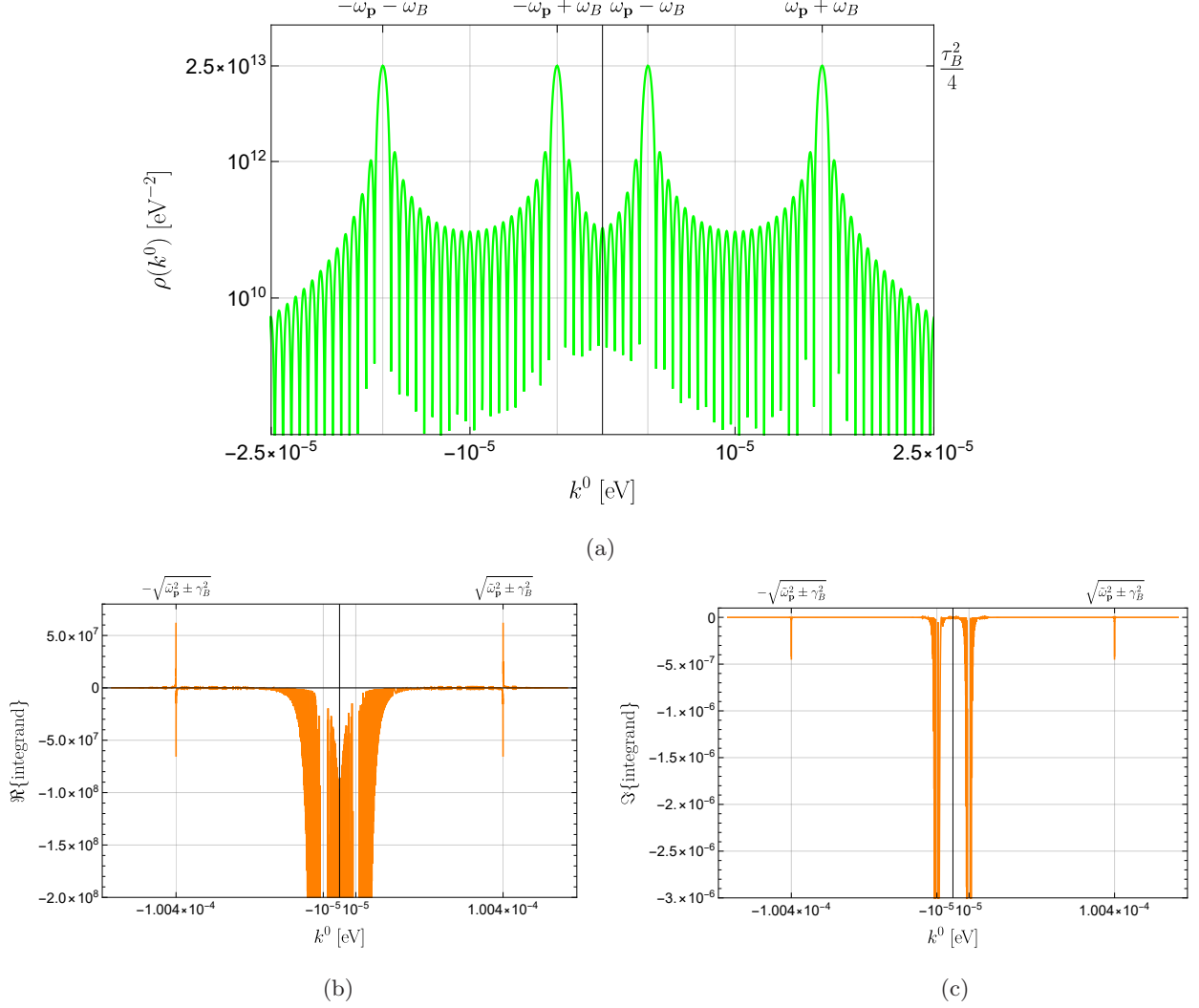


FIG. 4: (a) Profile function for $\omega_{\mathbf{p}} = 10^{-5}$ eV and $\omega_B = 10$ GHz. By reducing the ω_B , two peaks get closer to each other. (b) The real part and (c) the imaginary part of the integrand in (29) for $\omega_{\mathbf{p}} = 10^{-5}$ eV, $\omega_B = 100$ KHz, $m = 10^{-4}$ eV, and $g_{a\gamma\gamma} = 10^{-10}$ GeV^{-1} . Note that in these plot γ_B is a very small parameter.

the integration over k^0 in (29) close to the poles as follows

$$\begin{aligned}
 \left. \frac{\varphi}{G_a \omega_{\mathbf{p}}} \right|_{\text{from poles of propagator}} &= \text{not enhanced} + \frac{\rho(-\tilde{\omega}_{\mathbf{p}})}{-2\tilde{\omega}_{\mathbf{p}}} \int_{-\tilde{\omega}_{\mathbf{p}}-\epsilon}^{-\tilde{\omega}_{\mathbf{p}}+\epsilon} \frac{dk^0}{k^0 + \tilde{\omega}_{\mathbf{p}} - i\gamma_B/(2\tilde{\omega}_{\mathbf{p}})} \\
 &+ \frac{\rho(\tilde{\omega}_{\mathbf{p}})}{2\tilde{\omega}_{\mathbf{p}}} \int_{\tilde{\omega}_{\mathbf{p}}-\epsilon}^{\tilde{\omega}_{\mathbf{p}}+\epsilon} \frac{dk^0}{k^0 - \tilde{\omega}_{\mathbf{p}} + i\gamma_B/(2\tilde{\omega}_{\mathbf{p}})} \\
 &= \text{not enhanced} - \frac{2i\epsilon}{\gamma_B} [\rho(\tilde{\omega}_{\mathbf{p}}) + \rho(-\tilde{\omega}_{\mathbf{p}})] , \tag{31}
 \end{aligned}$$

where ϵ identifies areas that are close enough to the poles in a way that $\epsilon \ll \gamma_B$, and “not enhanced” denotes the contribution that is not enhanced by the presence of the poles. In this expression, the

real part is explicitly canceled after integrating around the side peaks. The imaginary part of (22) is non-vanishing. Since the profile function $\rho(k^0)$ is an even function of k^0 , the final expression for the imaginary part becomes $2\epsilon\rho(\tilde{\omega}_{\mathbf{p}})/\gamma_B$. The resulting expression in (31) is small and so we neglect it.

We then proceed by providing an analytical expression for the integration around the peaks produced by the profile function. This approach provides a simple analytic form for the impact of the near resonance phenomenon on the phase and the amplitude of the output signal. To approximate the integration (29) around these peaks we note the presence of the sinc functions, emerging from inserting (16) and (17) into (22), and then in (29). These sinc functions can be approximated with Dirac delta functions,

$$\frac{\sin(k^0 - \omega)\tau_B/2}{(k^0 - \omega)} \rightarrow \pi\delta(k^0 - \omega) , \quad (32)$$

where ω is any of $\pm(\omega_{\mathbf{p}} \pm \omega_B)$, and where the approximation holds in the limit of $\omega\tau_B \gg 1$. Given that the integral becomes important around the location of peaks, one can evaluate the integration (29) as

$$\frac{\varphi}{G_a\omega_{\mathbf{p}}} \simeq \frac{\pi\tau_B/2}{\epsilon_+ + i\gamma_B} + \frac{\pi\tau_B/2}{\epsilon_- + i\gamma_B} , \quad (33)$$

where

$$\epsilon_{\pm} = \omega_B(\omega_B \pm 2\omega_{\mathbf{p}}) - m_a^2 . \quad (34)$$

The imaginary part of (33) is small and it is neglected. In Fig (5), we have plotted the real part of the expression (33) in terms of m_a and $\omega_{\mathbf{p}}$ for $g_{a\gamma\gamma} = 10^{-10} \text{ GeV}^{-1}$ and compared it with numerical results. The results show a perfect agreement between the analytical expression given by (33) and a full numerical computation. In the following, we evaluate Eqs. (26) numerically, and we obtain the region in the axion mass-coupling plane that can be probed by our proposed experiment.

IV. Sensitivity to the axion-photon coupling

In this section, we estimate the sensitivity of our proposed experiment to the axion-photon coupling constant $g_{a\gamma\gamma}$ for a given ALP mass m_a . The configuration of our setup leads to a phase and amplitude modification in the cavity polarization mode which is aligned with the external magnetic field and leaves the perpendicular polarization intact. We exploit this property for the detection of the axion-induced phase with a noise cancellation mechanism. To this end, both

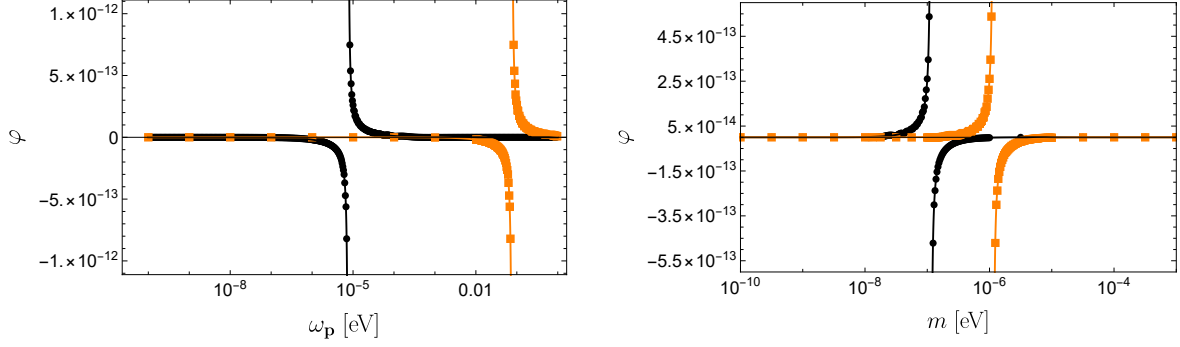


FIG. 5: Comparison of numerical calculation of φ integration on \mathcal{F} (markers) with its analytical approximation given in Eq. (33) (solid lines), in terms of ω_p (left panel) and m (right panel). The black and the orange curves in the left panel correspond to $m_a = 10^{-7}$ eV and $m_a = 10^{-5}$ eV, respectively. In the right one, the black and orange curves represent $\omega_p = 10^{-5}$ eV and $\omega_p = 10^{-3}$ eV, respectively. The coupling constant supposed to be $g_{a\gamma\gamma} = 10^{-10} \text{ GeV}^{-1}$.

polarization modes are equally pumped with the same laser pulse and a Homodyne measurement is performed on the outgoing cavity field. The phase difference between the two polarizations thus signals the photon-axion interaction in the presence of the magnetic field. The perpendicular polarization mode (here a_2) is employed as a reliable phase reference. Note that since both cavity modes are pumped by the same optical drive and go through the same optical path inside the cavity, they share the laser phase noise as well as the thermal noise imposed from vibrations of the cavity walls. Therefore, the homodyne phase difference setup shown in Fig. (3) cancels such joint phase fluctuation effects [34]. In the homodyne detection, one is only interested in the phase difference

$$\phi_{12}(t) = |\arg \langle a_1^{\text{out}}(t) \rangle - \arg \langle a_2^{\text{out}}(t) \rangle|, \quad (35)$$

where $\langle \cdot \rangle$ denotes the expectation value and $\arg(\alpha) \equiv \arctan(\Im\{\alpha\}/\Re\{\alpha\})$ gives the phase of α , a complex number. Here, the output cavity field is given by [37]

$$a_i^{\text{out}} = \sqrt{2\kappa} a_i - a_i^{\text{in}}. \quad (36)$$

In the following analysis, we employ a laser pulse with Gaussian envelope. Hence, the first moment of the input field operator for both polarizations is given by

$$\langle a_i^{\text{in}}(t) \rangle = \sqrt{\frac{P_L}{2\omega_p}} e^{-(t/\tau_L)^2} e^{-i\omega_p t}, \quad (37)$$

where P_L denotes the input laser power and τ_L is the length of the pulse. If long enough laser pulses ($\tau_L \gg \tau, \tau_B$) are employed for pumping the cavity modes, the phase shift $\phi_{12}(t)$ keeps accumulating,

while the oscillating background magnetic field is on. Then, the phase difference is maximum at the time $t = \tau_B/2$, when the external magnetic field is shut off.

The phase sensitivity in a single-shot optical scheme depends on the number of photons inside the probe and the uncertainty in its phase $\Delta\phi$. The larger number of photons, the higher becomes the minimum detectable phase. Nonetheless, there is a fundamental limitation in the width of an optical state in the corresponding phase space which imposes the standard quantum limit $\Delta\phi = 1$. The limit can be surpassed by modifying the optical field in a way that leads to the squeezing of its phase space representation along the phase direction, see Fig. (2). Such states are created via nonlinear optical crystals and are usually parameterized by r , the squeezing parameter such that $\Delta\phi = e^{-r}$. Hence, the single-shot sensitivity is $\delta\phi = \frac{e^{-r}}{\sqrt{N_{\text{ph}}}}$, where $r = 0$ gives the shot-noise limit. One repeats the measurement N_{exp} times to attain the higher sensitivity of $\delta\phi = \frac{e^{-r}}{\sqrt{N_{\text{ph}}N_{\text{exp}}}}$. The number of photons inside the cavity depends on the laser power P_L , the cavity decay rate κ , and the pulse duration τ_L . The number of photons contributing in the homodyne detection is given by $N_{\text{ph}} = |\langle a_1^{\text{out}} \rangle|^2 \approx |\langle a_2^{\text{out}} \rangle|^2$, where we have assumed that the effect of \mathcal{F}_i on the amplitude of a_1 is negligible. This assumption is supported by our numerical analysis. We thus have

$$\delta\phi(t) = \frac{e^{-r}}{|\langle a_1^{\text{out}}(t) \rangle| \sqrt{N_{\text{exp}}}}.$$

Detection of any phase difference then requires $\phi_{12}(t) > \delta\phi(t)$. Therefore, by introducing the cavity phase-amplitude parameter $\Phi \equiv |\langle a_1^{\text{out}}(\frac{\tau_B}{2}) \rangle| \phi_{12}(\frac{\tau_B}{2})$ the detection condition becomes:

$$\Phi > \frac{e^{-r}}{\sqrt{N_{\text{exp}}}}. \quad (38)$$

We evaluate Φ by numerically computing $\langle a_1 \rangle$ and $\langle a_2 \rangle$ from Eqs. (26) and (37) and then plugging the solutions in Eq. (36). For each value of ALP mass, we consider various laser frequencies to find the optimal one by which Φ gets maximized. It should be noticed that just $\omega_{\mathbf{p}} = n\text{FSR}$, ($n = 1, 2, 3, \dots$) are allowed for resonant laser frequencies. We find out by numerical inspection that the best signal is achieved when the following resonance condition is satisfied

$$m_a^2 + \omega_{\mathbf{p}}^2 = (\omega_B + \omega_{\mathbf{p}})^2. \quad (39)$$

From now on, we choose the laser frequency $\omega_{\mathbf{p}}$ such that it satisfies the above resonance equation and yet is on resonance with one of the cavity normal frequencies.

Fig. (6) shows the areas that can be excluded by our scheme. In the following analysis, we use a laser device with the power of $P_L = 100$ mW. We consider a squeezed light with the squeezing parameter $r \approx 1.75$ dB as well as a coherent state source ($r = 0$). Furthermore, a moderate

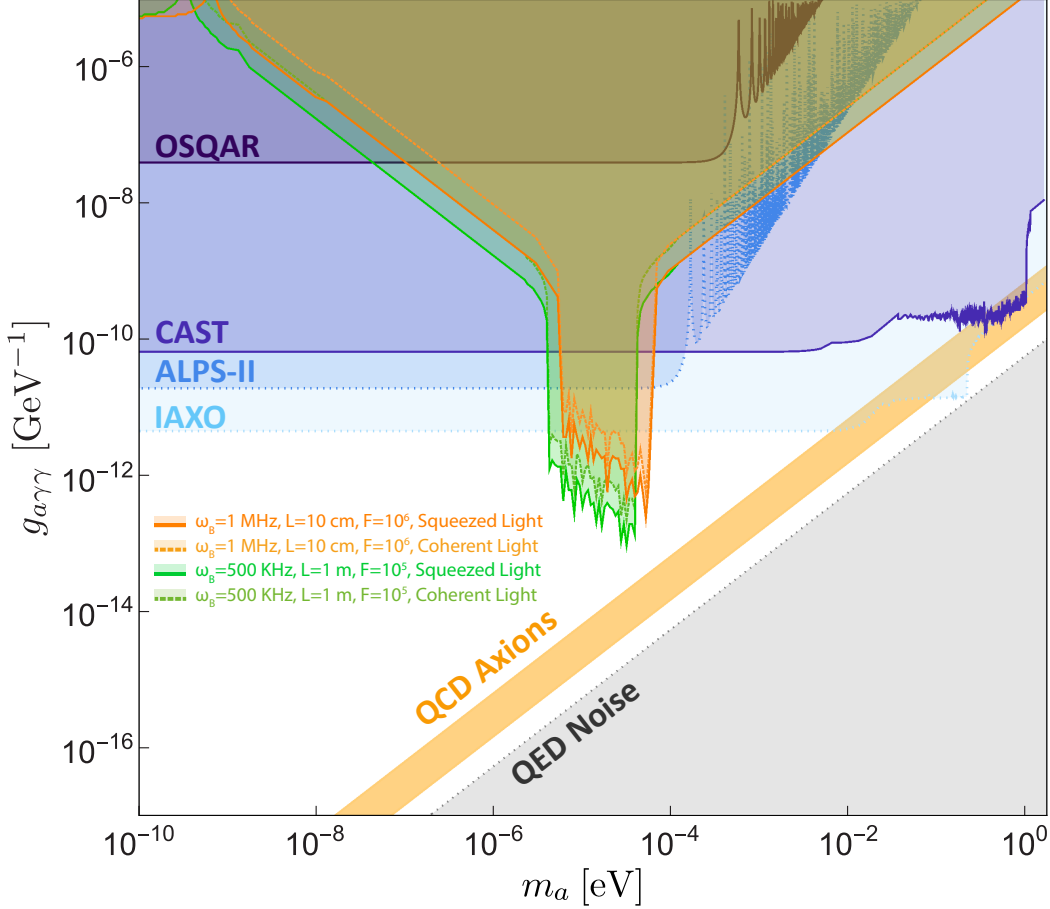


FIG. 6: Exclusion areas in the plane of ALP mass and axion-photon coupling constant for two different scenarios discussed in the text. The gray shade is the region where QED-induced polarization-flip dominates that of axion-induced processes [27]. The magnetic field's amplitude and the laser power are assumed to be $B_0 = 10$ T and 100 mW, respectively. The orange (green) solid line corresponds to a cavity with $L_x = 10$ cm ($L_x = 1$ m) which is exposed to $\omega_B = 1$ MHz ($\omega_B = 100$ KHz) oscillating magnetic field. Dashed lines show the limit of using coherent light instead of squeezed one.

magnetic field with $B_0 = 10$ T is taken into account in our analysis. We apply our scheme to two scenarios: one with cavity length $L_x = 10$ cm accompanied with $\omega_B = 1$ MHz for the magnetic field frequency. In the other scenario, we consider $L_x = 1$ m with $\omega_B = 500$ kHz to indicate the dependence of the exclusion region on the cavity length and the magnetic field frequency. It is also worth remarking that in our analysis we assume that the interaction time scale is smaller than the photon lifetime τ . Hence, we choose the parameters such that the inequality $\tau_B < \tau$ always holds.

In the first scenario, we have a $L_x = 10$ cm cavity with the finesse of $F = 10^6$ so the photon lifetime is $\tau = \frac{L_x F}{\pi c} \approx 1.61 \times 10^{11}$ eV. Considering $\omega_B = 1$ MHz for the oscillating magnetic field and $n = 16$ we have $\tau_B = (2n + 1)\pi/\omega_B \approx 1.57 \times 10^{11}$ eV so $\tau_B/\tau = 0.97$. In order to obtain

the optimal value of $\omega_{\mathbf{p}}$, Eq. (39) is solved for each m_a and the nearest integer multiple of FSR is picked up within the range of $0.03 \text{ eV} \leq \omega_{\mathbf{p}} \leq 3 \text{ eV}$. Note that this restriction comes from the accuracy of the homodyne detection scheme. We use the analytical integration in Eq. (33) and numerically solve the expectation values from Langevin equations in Eqs. (26). The results are plugged in Eq. (36) and then by applying Eq. (38) the resulting exclusion region is found which is illustrated in Fig. (6) with orange lines. The solid and dashed lines correspond to the squeezed and coherent light pumps, respectively. The same procedure is used for the second scenario with a $L_x = 1 \text{ m}$ cavity, $F = 10^5$, $\omega_B = 500 \text{ KHz}$, and $n = 7$ which leads to $\tau_B/\tau = 0.88$. The excluded area of this scenario is also shown in Fig. (6) with green lines.

According to Eq. (39), by employing cavity mode frequencies $0.03 \text{ eV} \leq \omega_{\mathbf{p}} \leq 3 \text{ eV}$ the ALP mass range of $2 \times 10^{-6} \text{ eV}$ to $6.3 \times 10^{-5} \text{ eV}$ is covered by the scenarios considered in this work. The lighter ALP values are covered by reducing the magnetic field frequency. Also, increasing the cavity length, while keeping the product $L_x F$ fixed, enhances the sensitivity of our scheme.

In generating the exclusion regions, we have employed optical pulses with duration $\tau_L = 3\tau$ which is the optimal value found by inspection. This constitutes the main experiment duration factor. By considering the optical pulse duration and the homodyne detection we take $\tau_{\text{exp}} \sim 10\tau$ as an estimation for each run of the experiment. Taking into account the number of experiment repetition $N_{\text{exp}} = 10^6$, one finds $N_{\text{exp}}\tau_{\text{exp}} \approx 17 \text{ min}$ for the time that takes for excluding/detecting each ALP mass. Hence, in the time span of a month about 2500 mass values can be examined. Note that only ALP mass values that match the resonance condition in our setup can be efficiently tested. Hence, for covering a small range of m_a a cavity with tunable length should be employed.

V. Summary and Conclusion

In this paper, we have studied the interaction of cavity photons with a time-dependent external magnetic field mediated by off-shell axion-like particles. Starting from the S-matrix, we first derived an effective interaction Hamiltonian describing this process. Remarkably, we have found that the time-dependence of the external magnetic field gives rise to a significant enhancement in the coupling of the photon-axion interaction emerging in the effective Hamiltonian. We thus have proposed to take the advantage of this enhancement property in a novel tabletop experiment for the detection of possible ALPs in an unexplored parameter area of axion mass and coupling rate. Our scheme relies on the quantum assisted precision optical phase measurement.

By employing proper polarization, power, and duration laser drive pulses as well as setup

geometry, we have engineered a noise cancellation mechanism where the laser phase noise and mirror vibrational noises are canceled out in the homodyne measurement. All the facilities used in our proposed experiment are well within the current technology. Using our scheme, it may be possible to detect ALPs with much greater sensitivity. As shown in Fig. (6), over a particle mass range $2 \times 10^{-6} \text{ eV} \leq m_a \leq 6.3 \times 10^{-5} \text{ eV}$ we can measure the phase difference down to a photon-ALPs coupling constant of $g_{a\gamma\gamma} \sim 10^{-14} \text{ GeV}^{-1}$ that is about three orders of magnitude lower than the current limits on $g_{a\gamma\gamma}$. Additionally, if higher frequency oscillatory magnetic fields become available in the future, a larger area of the parameter space can be explored by our scheme.

Acknowledgments

M.Z. acknowledges financial support by the University of Padova under the MSCA Seal of Excellence @UniPD programme.

A. ALPs effective propagator

Now, we will focus on calculating the exact propagator $D(k^0)$. Fig. (7) shows the corrections to the propagator of ALPs. The effective propagator is given by

$$\begin{aligned} iD(k^0) &= \frac{i}{\omega_{\mathbf{k}}^2 - \mathbf{p}^2 - m_0^2} + \frac{i}{\omega_{\mathbf{k}}^2 - \mathbf{p}^2 - m_0^2} (-i\Pi_B(k^0)) \frac{i}{\omega_{\mathbf{k}}^2 - \mathbf{p}^2 - m_0^2} + \dots \\ &= \frac{i}{\omega_{\mathbf{k}}^2 - \mathbf{p}^2 - m_a^2 - i\text{Im}\Pi_B(k^0)} , \end{aligned} \quad (\text{A1})$$

where $\Pi_B(k^0)$ denotes the sum of all one-particle irreducible (1PI) diagrams including diagrams with two external time-dependent magnetic field lines and m_a is the physical axion mass. The imaginary part of $\Pi_B(k^0)$ can be identified as the conversion rate of axion into photon in the presence of the background magnetic field [27]

$$\text{Im}\Pi_B(k^0) = k^0 \Gamma_B(k^0) . \quad (\text{A2})$$

Therefore, we can write the propagator as

$$iD(k^0) = \frac{i}{\omega_{\mathbf{k}}^2 - \mathbf{p}^2 - m_a^2 + ik^0 \Gamma_B(k^0)} , \quad (\text{A3})$$

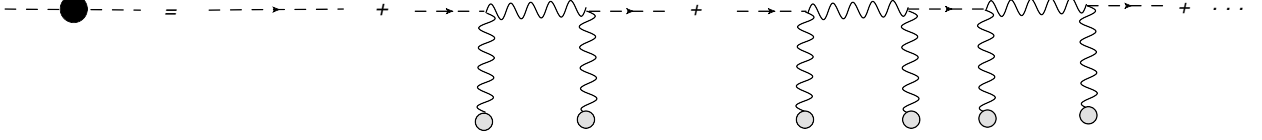


FIG. 7: Axion self energy in the presence of a time-dependent magnetic field.

B. ALPs decay rate in the background of a time-dependent magnetic field

In this section, we calculate the decay rate of axion in the presence of a time-dependent magnetic field. The amplitude for the axion-photon conversion process in the presence of the magnetic field is given by

$$\begin{aligned} \mathcal{T}_{fi} &= \langle a, \mathbf{k} | \frac{g_{a\gamma\gamma}}{2} \int d^4x \epsilon^{\mu\nu\rho\sigma} \phi(x) \bar{F}_{\rho\sigma}(x) \partial_\mu A_\nu(x) | \gamma, \mathbf{p} \rangle \\ &= -\frac{ig_{a\gamma\gamma}\sqrt{\omega_{\mathbf{p}}}}{V\sqrt{2k^0}} \int_{-\tau_B}^{\tau_B} dt e^{-i(\omega_{\mathbf{p}}-k^0)t} \int_V dx d^2\mathbf{x}_\perp \sin(p_x x) e^{-ik_x x} e^{i(\mathbf{p}_\perp - \mathbf{k}_\perp) \cdot \mathbf{x}_\perp} \boldsymbol{\varepsilon}(\mathbf{p}) \cdot \mathbf{B}(t) . \end{aligned} \quad (\text{B1})$$

Now, for a harmonic magnetic field $\mathbf{B}(t) = \mathbf{B}_0 \cos(\omega_B t)$, the conversion amplitude transforms to the form

$$\mathcal{T}_{fi} = -\frac{ig_{a\gamma\gamma}\sqrt{\omega_{\mathbf{p}}}\boldsymbol{\varepsilon}_s(\mathbf{p}) \cdot \mathbf{B}_0}{V\sqrt{2k^0}} \int_{-T/2}^{T/2} dt e^{-i(\omega_{\mathbf{p}}-k^0)t} \cos \omega_B t \int_V dx d^2\mathbf{x}_\perp \sin(p_x x) e^{-ik_x x} e^{i(\mathbf{p}_\perp - \mathbf{k}_\perp) \cdot \mathbf{x}_\perp} . \quad (\text{B2})$$

The conversion probability per unit time is given by

$$w = \frac{|\mathcal{T}_{fi}|^2}{T} = \frac{g_{a\gamma\gamma}^2 \omega_{\mathbf{p}}}{8L_y L_z \tau_B k^0} |\mathbf{B}_0|^2 P_1^2(k^0) (2\pi)^2 \delta^2(\mathbf{p}_\perp - \mathbf{k}_\perp) \delta_{p_x, k_x} , \quad (\text{B3})$$

in which we have ignored the boundary conditions for simplicity and also in a good approximation we have set $T = \tau_B$. The decay rate is given by

$$\Gamma_B(k^0) = \sum_{p_x} \int w \frac{L_y L_z d^2\mathbf{p}_\perp}{(2\pi)^2} = \frac{g_{a\gamma\gamma}^2 \omega_{\mathbf{p}}}{8k^0} |\mathbf{B}_0|^2 \frac{P_1^2(k^0)}{\tau_B} , \quad (\text{B4})$$

Approximating $P_1^2(k^0)/\tau_B \approx \tau_B/4$, we find a maximum value for the decay rate as

$$\Gamma_B^{\max} = \frac{g_{a\gamma\gamma}^2 \omega_{\mathbf{p}}}{32 k^0} |\mathbf{B}_0|^2 \tau_B . \quad (\text{B5})$$

C. A more feasible time-dependent magnetic field

In section II, we analyzed the effects of a time-dependent magnetic field with a rectangular profile function $\Pi(t/\tau_B)$. We investigate a more practical profile that may be more feasible experimentally.

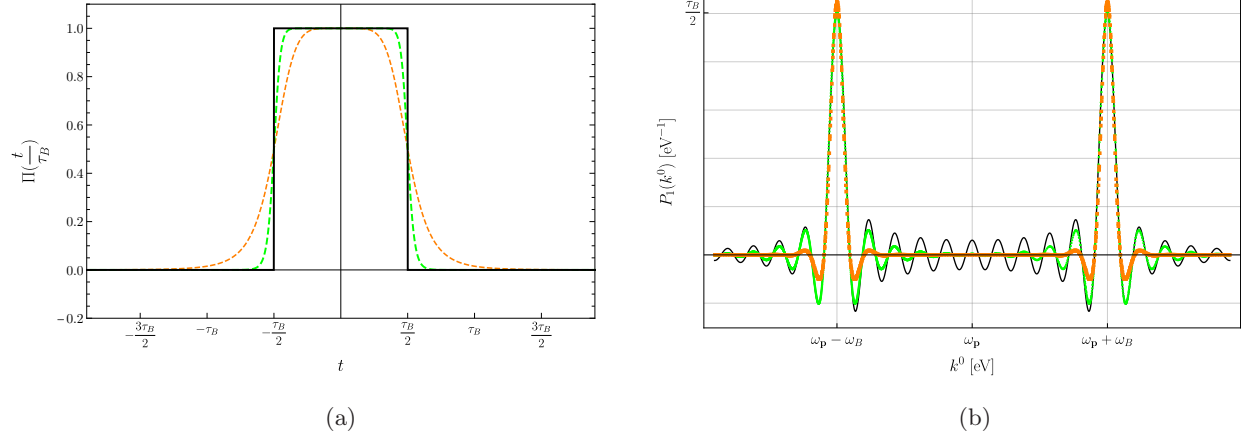


FIG. 8: (a) Comparison of the rectangular function $\Pi(t)$ (solid black) with its approximation in relation (C1). Dashed orange and long-dashed green curves belong to $n = 6$ and $n = 20$, respectively. (b) Effect of approximating rectangular function on first profile in (16). The solid black line is $P_1(k^0)$ with the exact rectangular function. Orange and green dotted curves belong to numerical calculation of $P_1(k^0)$ in which rectangular function in (C1) is approximated with $n = 6$ and $n = 20$, respectively.

To this end, we examine the following approximation of $\Pi(t)$

$$\Pi(t) = \lim_{n \rightarrow \infty} \frac{1}{(2t)^n + 1}, \quad (\text{C1})$$

where n is a positive integer. It follows that the rectangular function $\Pi(t)$ can be approximated with high accuracy by taking sufficiently large integer n . The Fig. (8a) shows $\Pi(t/\tau_B)$ in comparison with the approximation function (C1) for $n = 6$ and $n = 20$. The larger the value of n , the more accurate agreement with the $\Pi(t/\tau_B)$ function. As discussed in the text, due to the presence of the $\Pi(t/\tau_B)$ function and after integrating over time in equations (16) and (17), the $P_1(k^0)$ and $P_2(k^0)$ are obtained in terms of the *sinc* functions. Here, we replace the $\Pi(t/\tau_B)$ with the approximation expression (C1) and once again calculated (16) and (17) numerically. In Fig. (8) we have displayed the results for $P_1(k^0)$ (a similar result is obtained for $P_2(k^0)$). As this figure shows, if we replace the rectangular function with the approximate function (C1), the main shape of the peaks will not change. Therefore, we do not expect the main results obtained in the text to be affected by the values of n .

-
- [1] L. F. Abbott and P. Sikivie, “A Cosmological Bound on the Invisible Axion,” Phys. Lett. B **120**, 133-136 (1983).
 - [2] M. Dine and W. Fischler, “The Not So Harmless Axion,” Phys. Lett. B **120**, 137-141 (1983).

- [3] J. Preskill, M. B. Wise and F. Wilczek, “Cosmology of the Invisible Axion,” *Phys. Lett. B* **120**, 127-132 (1983).
- [4] R. D. Peccei and H. R. Quinn, “CP Conservation in the Presence of Instantons,” *Phys. Rev. Lett.* **38**, 1440-1443 (1977).
- [5] R. D. Peccei and H. R. Quinn, “Constraints Imposed by CP Conservation in the Presence of Instantons,” *Phys. Rev. D* **16**, 1791-1797 (1977).
- [6] S. Weinberg, “A New Light Boson?,” *Phys. Rev. Lett.* **40**, 223-226 (1978).
- [7] F. Wilczek, “Two Applications of Axion Electrodynamics,” *Phys. Rev. Lett.* **58**, 1799 (1987).
- [8] P. Sikivie, “Experimental Tests of the Invisible Axion,” *Phys. Rev. Lett.* **51**, 1415-1417 (1983).
- [9] P. Sikivie, “Detection Rates for ‘Invisible’ Axion Searches,” *Phys. Rev. D* **32**, 2988 (1985).
- [10] G. Raffelt and L. Stodolsky, “Mixing of the Photon with Low Mass Particles,” *Phys. Rev. D* **37**, 1237 (1988).
- [11] D. M. Lazarus, G. C. Smith, R. Cameron, A. C. Melissinos, G. Ruoso, Y. K. Semertzidis and F. A. Nezrick, “A Search for solar axions,” *Phys. Rev. Lett.* **69**, 2333-2336 (1992)
- [12] A. S. Chou *et al.* [GammeV (T-969)], “Search for axion-like particles using a variable baseline photon regeneration technique,” *Phys. Rev. Lett.* **100**, 080402 (2008) [arXiv:0710.3783 [hep-ex]].
- [13] C. Robilliard, R. Battesti, M. Fouche, J. Mauchain, A. M. Sautivet, F. Amiranoff and C. Rizzo, “No light shining through a wall,” *Phys. Rev. Lett.* **99**, 190403 (2007) [arXiv:0707.1296 [hep-ex]].
- [14] K. Ehret, M. Frede, S. Ghazaryan, M. Hildebrandt, E. A. Knabbe, D. Kracht, A. Lindner, J. List, T. Meier and N. Meyer, *et al.* “New ALPS Results on Hidden-Sector Lightweights,” *Phys. Lett. B* **689**, 149-155 (2010) [arXiv:1004.1313 [hep-ex]].
- [15] I. G. Irastorza and J. Redondo, “New experimental approaches in the search for axion-like particles,” *Prog. Part. Nucl. Phys.* **102**, 89-159 (2018) [arXiv:1801.08127 [hep-ph]].
- [16] P. Sikivie, “Invisible Axion Search Methods,” [arXiv:2003.02206 [hep-ph]].
- [17] A. C. Melissinos, “Search for Cosmic Axions using an Optical Interferometer,” *Phys. Rev. Lett.* **102**, 202001 (2009) [arXiv:0807.1092 [hep-ph]].
- [18] W. DeRocco and A. Hook, “Axion interferometry,” *Phys. Rev. D* **98**, no.3, 035021 (2018) [arXiv:1802.07273 [hep-ph]].
- [19] I. Obata, T. Fujita and Y. Michimura, “Optical Ring Cavity Search for Axion Dark Matter,” *Phys. Rev. Lett.* **121**, no.16, 161301 (2018) [arXiv:1805.11753 [astro-ph.CO]].
- [20] H. Liu, B. D. Elwood, M. Evans and J. Thaler, “Searching for Axion Dark Matter with Birefringent Cavities,” *Phys. Rev. D* **100**, no.2, 023548 (2019) [arXiv:1809.01656 [hep-ph]].
- [21] A. A. Geraci, C. Bradley, D. Gao, J. Weinstein and A. Derevianko, “Searching for Ultralight Dark Matter with Optical Cavities,” *Phys. Rev. Lett.* **123**, no.3, 031304 (2019) [arXiv:1808.00540 [astro-ph.IM]].
- [22] D. Harari and P. Sikivie, “Effects of a Nambu-Goldstone boson on the polarization of radio galaxies and the cosmic microwave background,” *Phys. Lett. B* **289**, 67-72 (1992).

- [23] M. Pospelov, A. Ritz, C. Skordis, A. Ritz and C. Skordis, “Pseudoscalar perturbations and polarization of the cosmic microwave background,” *Phys. Rev. Lett.* **103**, 051302 (2009) [arXiv:0808.0673 [astro-ph]].
- [24] F. Finelli and M. Galaverni, “Rotation of Linear Polarization Plane and Circular Polarization from Cosmological Pseudo-Scalar Fields,” *Phys. Rev. D* **79**, 063002 (2009) [arXiv:0802.4210 [astro-ph]].
- [25] G. Sigl and P. Trivedi, “Axion-like Dark Matter Constraints from CMB Birefringence,” [arXiv:1811.07873 [astro-ph.CO]].
- [26] M. A. Fedderke, P. W. Graham and S. Rajendran, “Axion Dark Matter Detection with CMB Polarization,” *Phys. Rev. D* **100**, no.1, 015040 (2019) [arXiv:1903.02666 [astro-ph.CO]].
- [27] M. Zarei, S. Shakeri, M. Abdi, D. J. E. Marsh and S. Matarrese, “Probing Virtual Axion-Like Particles by Precision Phase Measurements,” [arXiv:1910.09973 [hep-ph]].
- [28] A. Kosowsky, “Cosmic microwave background polarization,” *Annals Phys.* **246**, 49-85 (1996) doi:10.1006/aphy.1996.0020 [arXiv:astro-ph/9501045 [astro-ph]].
- [29] E. Bavarsad, M. Haghighat, Z. Rezaei, R. Mohammadi, I. Motie and M. Zarei, “Generation of circular polarization of the CMB,” *Phys. Rev. D* **81**, 084035 (2010) doi:10.1103/PhysRevD.81.084035 [arXiv:0912.2993 [hep-th]].
- [30] N. Bartolo, A. Hoseinpour, G. Orlando, S. Matarrese and M. Zarei, “Photon-graviton scattering: A new way to detect anisotropic gravitational waves?,” *Phys. Rev. D* **98**, no.2, 023518 (2018) doi:10.1103/PhysRevD.98.023518 [arXiv:1804.06298 [gr-qc]].
- [31] N. Bartolo, A. Hoseinpour, S. Matarrese, G. Orlando and M. Zarei, “CMB Circular and B-mode Polarization from New Interactions,” *Phys. Rev. D* **100**, no.4, 043516 (2019) doi:10.1103/PhysRevD.100.043516 [arXiv:1903.04578 [hep-ph]].
- [32] A. Hoseinpour, M. Zarei, G. Orlando, N. Bartolo and S. Matarrese, “CMB V modes from photon-photon forward scattering revisited,” *Phys. Rev. D* **102**, no.6, 063501 (2020) doi:10.1103/PhysRevD.102.063501 [arXiv:2006.14418 [hep-ph]].
- [33] G. Breit and E. Wigner, *Phys. Rev.* **49**, 519-531 (1936) doi:10.1103/PhysRev.49.519
- [34] C. W. Gardiner, P. Zoller, *Quantum Noise*, (Springer, Berlin, 2004).
- [35] K. Kakazu, Y. S. Kim, “Quantization of electromagnetic fields in cavities and spontaneous emission,” *Phys. Rev. A* **50**, 1830 (1994).
- [36] C. W. Gardiner, M. J. Collett, “Input and output in damped quantum systems: Quantum stochastic differential equations and the master equation,” *Phys. Rev. A* **31** (1985) 3761.
- [37] D. F. Walls and G. J. Milburn, *Quantum Optics* (Springer, Berlin, 2006).